Stars and planets at high spatial and spectral resolution

Albrecht, S.

Chapter 3

MWC 349A

In this chapter we aim to understand the massive young stellar object MWC 349A better, by studying the structure of its disk, the structure of the region from where the hydrogen emission lines originate and the forbidden lines at high spatial resolution in the N-band.

Previous observations of this peculiar emission line star suggest that it is a young massive star in the short-lived phase during which it has already dissipated its parent cloud, but it is still surrounded by the accretion disk which is seen nearly edge-on. It is believed that the unique hydrogen recombination line maser/laser activity of MWC 349A from mm to infrared wavelengths is also a consequence of this viewing angle. However, despite a wealth of data already available, it has so far not been possible to assign a clear evolutionary status to MWC 349A.

We have used the unique capabilities of the Very Large Telescope Interferometer (VLTI) in combination with the Mid-Infrared Interferometric Instrument (MIDI) to observe MWC 349A and spatially resolve the inner parts of its disk. We observed MWC 349A with MIDI at the peak of its spectral energy distribution, from 8 to 13 μm, with a spectral resolution of R $\sim$ 230. We obtained 19 *u,v* points with different baseline lengths and at different position angles.

The observed wavelength-dependence of the continuum visibility amplitudes agrees with model calculations for a hot inner disk and a wider colder disk both seen edge on. We model the visibility amplitudes and the SED in the spectral wavelength range of MIDI with optically thin emission from warm silicate, and a shield of colder material. This is critical to obtain a good agreement between model and data. In addition the signatures of at least a dozen emission lines have been identified in the interferometric data. We extract the visibilities of these lines, and model the spatial distribution of the emitting regions successfully using two emission regions separated by a few tens of mas consistent with observations of hydrogen masers at radio wavelengths.

S. Albrecht, R. N. Tubbs, A. Quirrenbach & I.A.G. Snellen
A&A in preparation

3.1 Introduction MWC 349A

Although in the optical MWC 349A is a rather inconspicuous early-type emission line star, it is very bright throughout the infrared, and it is one of the most luminous radio stars known to date (Altenhoff et al. 1994; Baldwin et al. 1973). Its bolometric luminosity is at least $2{\cdot}10^4\,L_\odot$, if corrected for foreground extinction, but probably much higher if much of the absorbing material is in a disk allowing most of the stellar radiation to escape. A luminosity as high as $5 \cdot 10^5\,L_\odot$ appears plausible if a bolometric correction corresponding to a hot main sequence star is applied. Recent spectropolarimetric observations have strengthened the classification of MWC 349A as a pre-main sequence B[e] star (Meyer et al. 2002). Furthermore, direct evidence for a circumstellar disk was obtained from high-resolution VLA images (White & Becker 1985; Martín-Pintado et al. 1993; Tafoya et al. 2004) and from near-infrared spectroscopy (Hamann & Simon 1986). The hydrogen recombination line maser detected in this source by Martin-Pintado et al. (1989) is expected to originate from this disk (Planesas et al. 1992; Thum et al. 1992). The latter authors suggest, on the basis of a series of maser transitions at 1 and 2 mm wavelength, that the disk is in Keplerian rotation around a central mass of $30\,M_\odot$, which would indicate that the central star is of spectra type O6-O8, if it is not a close binary.

The remarkable stability of the double-peaked maser features (Thum et al. 1992; Gordon 1992; Thum et al. 1994a,b) and the evidence for Keplerian rotation prompted Thum & Martin-Pintado (1994) to propose that MWC 349A is a young massive star, near the zero-age main sequence, still surrounded by its accretion disk. In this picture, we observe MWC 349A in the (probably short) period of a massive star's life, during which the parental cloud is already completely dispersed, but the star has not yet fully destroyed its accretion disk by ionization. Indeed, the spectral energy distribution (SED) shows no trace of significant cold dust emission. This is unlike the SED of compact H II regions which invariably peak near $70\,\mu$m, owing to the presence of a large mass of cold dust in the parental cloud. The extremely uniform slope of the SED out to the longest radio wavelengths is also evidence for a constant-velocity ionized wind which expands isotropically into the surrounding volume, which it appears to have cleared out to at least 0.1 pc. The extinction towards the central emission-line source is comparatively small ($A_V \sim 10$ mag), indicating that MWC 349A has left its parent molecular cloud, enabling studies of this object in the far red and infrared. Emission-line spectra in this wavelength regime have been successfully interpreted by a photo-evaporating disk model (Hamann & Simon 1986). While the outer regions of the disk consist of cold, dense neutral gas, the inner few AU are photo-ionized by the UV flux from the central star. A host of fine-structure lines from ions with ionization potentials of up to 41 eV are detected in the Infrared Space Observatory (ISO) spectrum of MWC 349A, confirming that the effective temperature of the star is at least 35,000 K (Quirrenbach et al. 2001). Hydrogen and He I recombination lines seem to be generated in a wind emanating from the disk surface rather than from the stellar photosphere, indicating substantial illumination of the disk by scattered UV radiation. The H II region generated in this way should be fairly long-lived (about $3{\cdot}10^5$ years), because it is constantly replenished from the disk, which provides an abundant reservoir of dense gas. The strong radio continuum emission originates in a massive ionized wind ($1.2{\cdot}10^{-5}\,M_\odot\,\mathrm{yr}^{-1}$). Its low expansion velocity of 50 km s^{-1} testifies to its origin on the circumstellar disk (not the stellar photosphere). MWC 349A is therefore considered as the prime example of a photo-evaporating disk around a massive star.

The most spectacular features of the MWC 349A disk are the strong hydrogen recombina-

tion line masers at mm and sub-mm wavelengths (H21α to H35α), which are thought to be located in the disk at 40 AU distance (Martin-Pintado et al. 1989; Thum et al. 1994b). In the mid-1990s MWC 349A was observed with the Short Wavelength Spectrograph (SWS) and Long Wavelength Spectrograph (LWS) grating spectrometers on the ISO satellite (Thum et al. 1998; Quirrenbach et al. 2001). Among the about 100 detected hydrogen recombination lines are all 12 transitions within the wavelength range accessible to ISO, from Brα at 4.05 μm to H15α at 169.4 μm. The lines with n < 6 are optically thick; the lines with higher n are amplified, and thus constitute infrared lasers. Combining the ISO results with millimeter and sub-millimeter data gives the first global view of the recombination line laser/maser phenomenon in this star. The maximum line-integrated amplification, of a factor of 30, occurs in the region near n = 19 at 300 μm.

Complementary information on the MWC 349A disk comes from recent high spatial resolution observations in the near-infrared using aperture masking at the Keck I Telescope (Danchi et al. 2001), and speckle interferometry at the SAO 6 m Telescope (Hofmann et al. 2002). These data sets reveal a disk seen almost edge-on at a position angle of $100^\circ \pm 3^\circ$ on the sky, consistent with the position angle of a dark lane observed previously in the VLA continuum maps. It therefore appears that the uniqueness of MWC 349A (the only known hydrogen recombination line maser source known to date) is a consequence of its being in a short-lived evolutionary stage, combined with an almost edge-on orientation.

Observing MWC 349A with MIDI and the VLTI we want to investigate the structure of the inner circumstellar disk. Taking advantage of the spectral resolution of MIDI in the N band we further want to investigate the mineralogy of the disk and the hydrogen emission lines visible in the N band.

3.2 MIDI Observations

We observed MWC 349A with the MIDI instrument of the VLTI (Leinert et al. 2003). We obtained five (u, v) data points on the 47 m long baseline between the Unit Telescopes UT2 and UT3 during the first half-night of May 26 2005, and six (u, v) data points on the 102 m UT1-UT3 baseline during the second half-night of May 27 2008. Unfortunately, four of these observations were affected by rather thick cirrus, and cannot be used. All these observations were obtained in High_Sens mode, meaning that no simultaneous photometric measurement of beams before combination is done, i.e. measurements of the correlated and uncorrelated flux are carried out sequentially. This requires that the transfer function of Earth's atmosphere does not change significantly between the two observations. Unfortunately, this condition was not met for the observations affected by cirrus clouds. Two additional (u, v) data points were obtained on the baselines UT2-UT4 (89 m length) and UT3- UT4 (62 m). These two baselines provide data at a somewhat different position angle. These observations were also obtained in MIDI's High_-Sens mode, and like the former observations they also employed the GRISM, which provides spectrally resolved data R $(\lambda/\Delta\lambda) \sim 230$ from 8 μm to 13 μm. These observations provide information on small spatial scale structures in MWC 349A (down to a few mas).

To further complement these observations and to obtain information on larger scales, we also observed with shorter baselines using the Auxiliary telescopes (ATs), as these can be positioned closer to each other than the UT's. Three (u, v) points were obtained with a 16 m baseline and

Table 3.1 — Log of MIDI observations of MWC 349A.

Date	Baseline	number (u,v) points	Dispersive element	Mode
26-05-2005	UT2 - UT3	5	GRISM	High_Sens
27-05-2005	UT1 - UT3	6	GRISM	High_Sens
20-07-2005	UT3 - UT4	1	GRISM	High_Sens
24-08-2005	UT2 - UT4	1	GRISM	High_Sens
26-05-2006	E0 - G0	2	PRISM	Sci_Phot
18-06-2006	E0 - G0	2	PRISM	Sci_Phot
16-06-2006	G0 - H0	3	PRISM	Sci_Phot

NOTES – See http://www.eso.org/sci/facilities/paranal/telescopes/vlti/configuration/index.html for the positions of the different telescopes / AT stations at Paranal observatory.

three observations with a 32 m baseline, all again with slightly varying position angles. These six observations were obtained in Sci_Phot mode of MIDI using the PRISM as the dispersive element, giving a modest spectral resolution of $R \sim 30$. In the Sci_Phot mode the correlated and uncorrelated flux are obtained simultaneously at different locations on the detector. The (u,v) plane coverage of the MIDI observations is shown in Figure 3.1. All observations are listed in Table 3.1.

For the reduction of all MIDI data the software package MIA+EWS 1.5.2[1] was used. The quantities measured by MIDI are the visibility amplitude and the visibility phase. The visibility amplitude delivered by MIDI is the uncalibrated *instrumental* visibility amplitude. As the transfer function of MIDI delivers a visibility amplitude for a point source which is $\lesssim 1$, and the transfer function might change over time, each measurement of MWC 349A is accompanied by a calibrator observation, either directly before or after the observation of the science target. To derive the calibrated visibility amplitudes, the observed amplitude is divided by the visibility amplitude of the calibrator star (assumed to be unresolved). A second assumption, which is implicitly made for these observations, is that the transfer function of the Earth's atmosphere does not change over the time span between the observations of the calibrator and science target. In addition, it is also assumed that the Earth's atmosphere has the same transfer function towards the different stars being observed in different parts of the sky. For MIDI it is often the case that the angle between calibrator and the science object is considerable (see the positions of the calibrator stars and science objects in Table A.1). It turns out that the error terms induced by these assumptions constitute the largest error sources in the visibility amplitudes (MWC 349A is very bright in the N band which reduces the importance of other error sources). We therefore collected all calibrator observations made during the nights on which MWC 349A was observed, from the ESO archive, and compared the scatter in their visibility amplitudes to assess the uncertainty in the overall visibility amplitudes derived of MWC 349A. All visibility amplitudes

[1] http://www.strw.leidenuniv.nl/∼nevec/MIDI/index.html

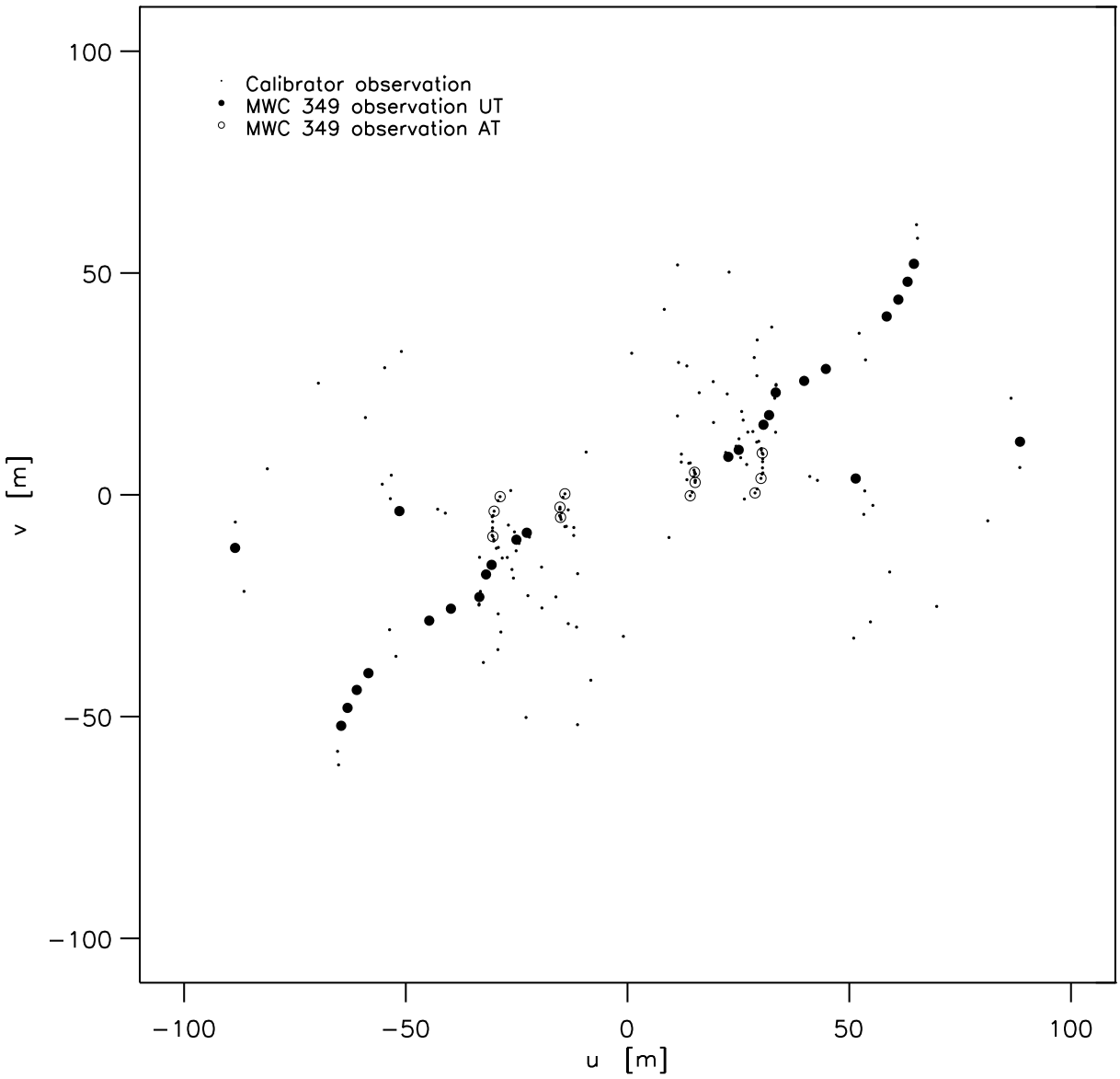

Figure 3.1 — The Fourier (*uv* plane) coverage of the MIDI observations. The filled circles indicate the *uv* position of the MWC 349A observations made with UTs. The open circles indicate the observations using the ATs. The small dots show all the calibrator observations done during the observation nights. Note that most observations are along one position angle in the *uv* plane. This is due to the high northern declination of the object and the resulting low elevation at which it is seen from Paranal. This means that MWC 349A is only observable for a short period each night and is always at about the same hour angle with a similar orientation of the UT1-UT3 and UT2-UT3 baselines.

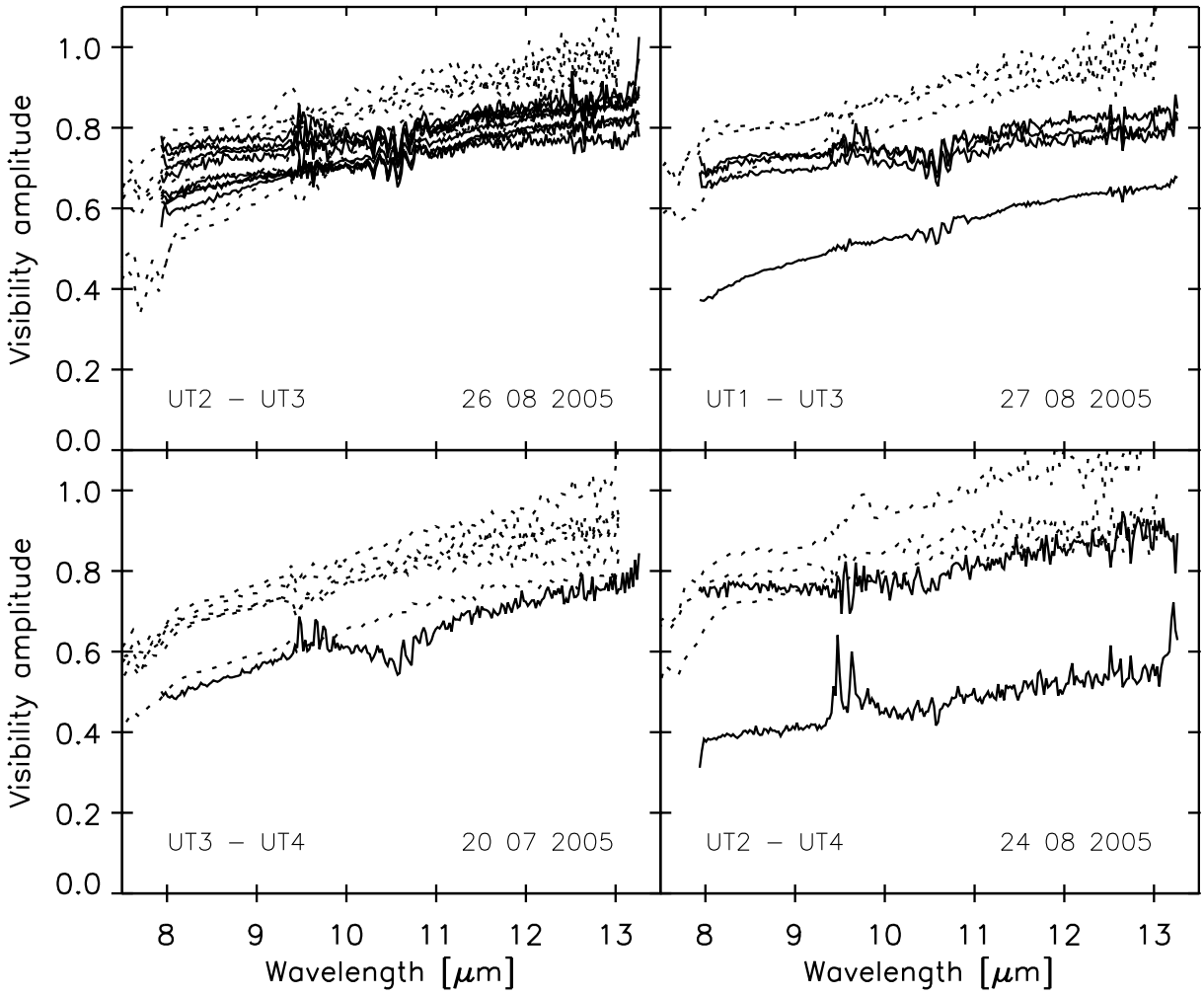

Figure 3.2 — The four panels show the visibility amplitudes of all calibrators observed using MIDI on four nights during which MWC 349A was also observed. The observing dates and baselines are indicated in the bottom right and left corners of each panel, respectively. The solid lines represent observations obtained in High_Sens mode using the GRISM as dispersive element. The dotted lines indicate High_-Sens PRISM observations.

of the calibrators can been seen in Figures 3.2 and 3.3. Note that 13 Lyr, one of the calibrators on the night 27.08.2005, is already partly resolved. The visibility amplitudes for the calibrator (γ Cyg) obtained in High_Sens mode during the night 24.08.2005 changes strongly between the two observations, which is probably due to changing atmospheric conditions. One can see in these figures that the transfer function of the instrument and the atmosphere is stable during most nights on a $\sim$ 10% level, while small systematic differences exists between the different instrumental setups. Note that the uncertainties derived in this way are for the overall visibility amplitude. The relative precision and accuracy of the visibility amplitudes at the different wavelengths is much higher. One example instrumental visibility amplitude of MWC 349A is displayed in Figure 3.4.

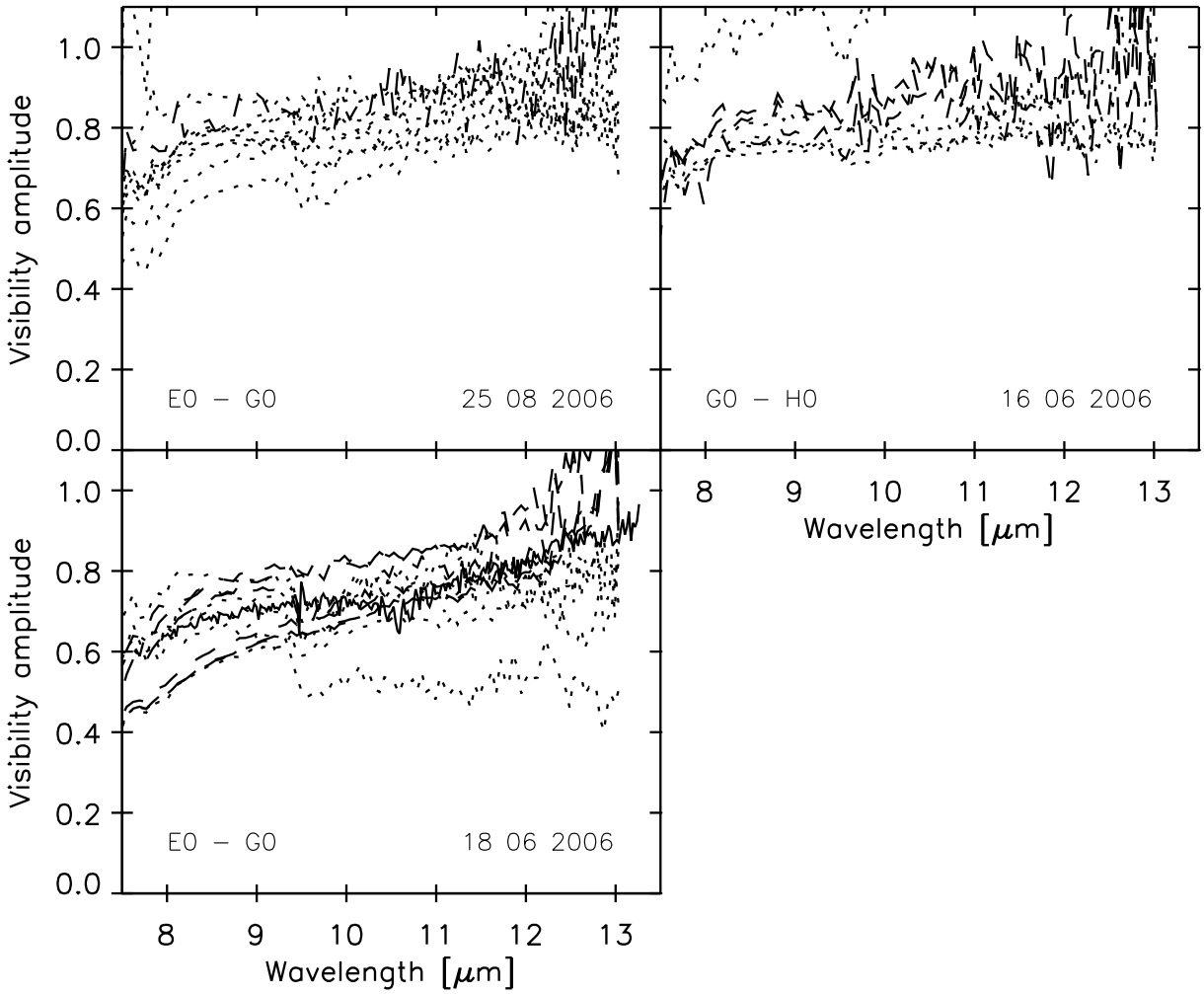

Figure 3.3 — The same as Figure 3.2 but for the three other nights. Sci_Phot PRISM observations of calibrators were also carried out on these nights, as shown by the dashed lines

The visibility phase is the second important quantity obtained from the MIDI measurements. The phase of the interferometric fringes contains information on the position of the emission well below the resolution limit (observing wavelength / projected baseline length) of the interferometer. To exploit this information an absolute phase reference is needed, which does not exist for the case of MIDI observations as the atmosphere corrupts the phase signal. The color-differential phase can however deliver information on the relative position of the centroid emission at the different wavelengths. The greater the difference between the wavelengths the larger the influence of the atmosphere, which makes the interpretation of the differential phase over the complete MIDI pass-band difficult. Fortunately, for measurements of rapid phase changes with wavelength the phase in the adjacent wavelength channels constitutes an excellent calibration source. See Figure 3.5 for an example differential phase as a function of wavelength for one (u, v) point. One can clearly see a change in phase at the wavelength of the forbidden [Ne II]

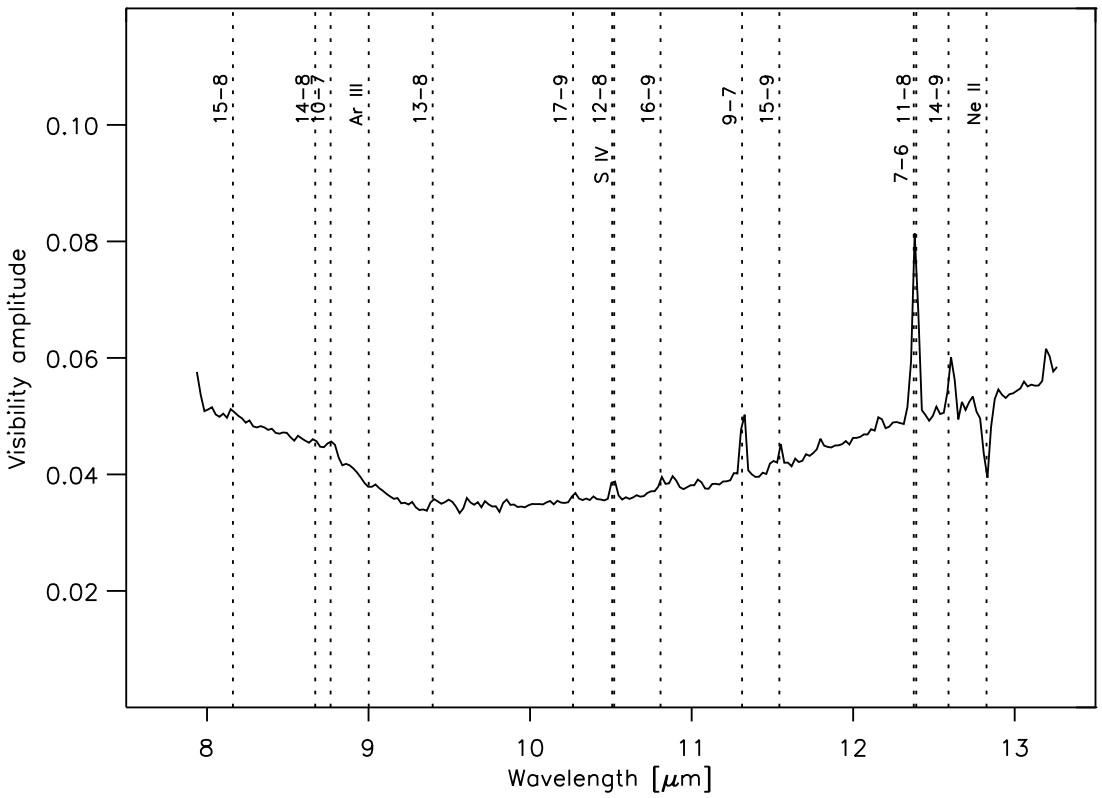

Figure 3.4 — Example of an instrumental visibility amplitude obtained with MIDI, for MWC 349A for a projected baseline of 48 m and a position angle of 33°. The observations were carried out in High_Sens GRISM mode ($R\sim$ 230 over the MIDI band-pass from 8 μm – 13 μm). The wavelengths of all hydrogen recombination lines in the MIDI passband and the forbidden lines are indicated.

line and the stronger hydrogen recombination lines. Note that one degree of phase corresponds to 1/360 th of the interferometer resolution, i.e., we are sensitive to displacements as small as 100 μas, which corresponds to 0.1 AU.

3.3 Results

3.3.1 The circumstellar disk

The visibility amplitudes for MWC 349A show a characteristic shape for all baselines (see Figures 3.6, 3.7, and 3.8). It is in general rather high at short wavelengths, drops to a minimum around 10 μm, and increases again towards the long-wavelength end of the spectrometer range.

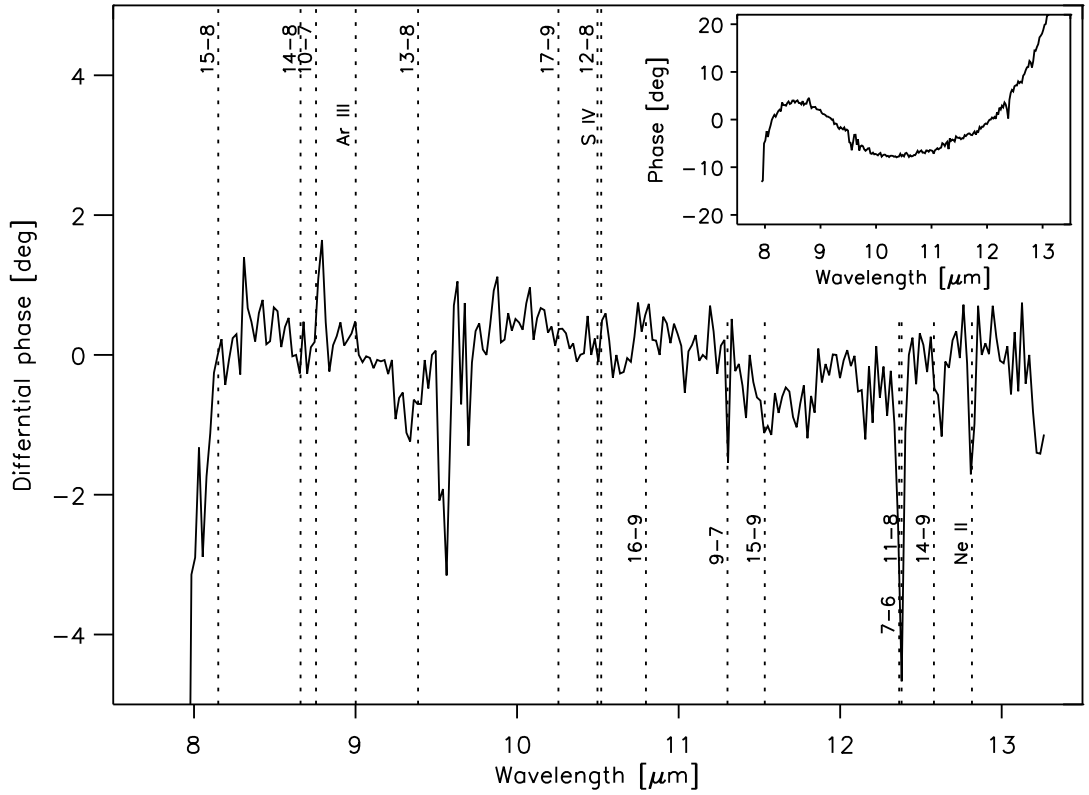

Figure 3.5 — The differential visibility phase as a function of wavelength for the same observations as shown in Figure 3.4. A high-pass filter was applied to the visibility phase to reject distortion due to dispersion in the air-filled light ducts in the interferometer, this will however also destroy all low frequency phase information on MWC 349A which might be present. The original phase can be seen in the insert. Note that as no absolute phase is defined, there is an arbitrary offset. The phases are unreliable in the 9.4 μm–9.9 μm region due to the influence of ozone in the Earth's atmosphere.

Visibilities with a somewhat similar wavelength dependence have been observed in a number of Herbig Ae/Be stars (e.g. Leinert et al. 2004). They are characteristic for disks, in which a warmer and smaller component dominates the shorter wavelengths within the N band, whose flux drops towards longer wavelengths, and a cooler, larger component whose contribution to the visibility becomes more important at longer wavelengths. The rise in visibility amplitude at long wavelengths is partly due to the reduced spatial resolution of the interferometer towards long wavelengths. The decrease in resolution of the interferometer with increasing observing wavelength might however not be the only reason for a rise in visibility amplitude at longer wavelengths. Mineralogy of the dust which constitutes the disk might play a role as well as geometric effects. The mass absorption coefficient (κ_ν) of amorphous silicate, which is thought to be abundant in proto-planetary disks, rises from the short wavelength side of the band-pass of MIDI, peaks at $\sim 9.7\,\mu$m, and subsequently decreases again (see Figure 3.9). That means one actually probes *colder* layers closer to the mid-plane of the circumstellar disk at the long

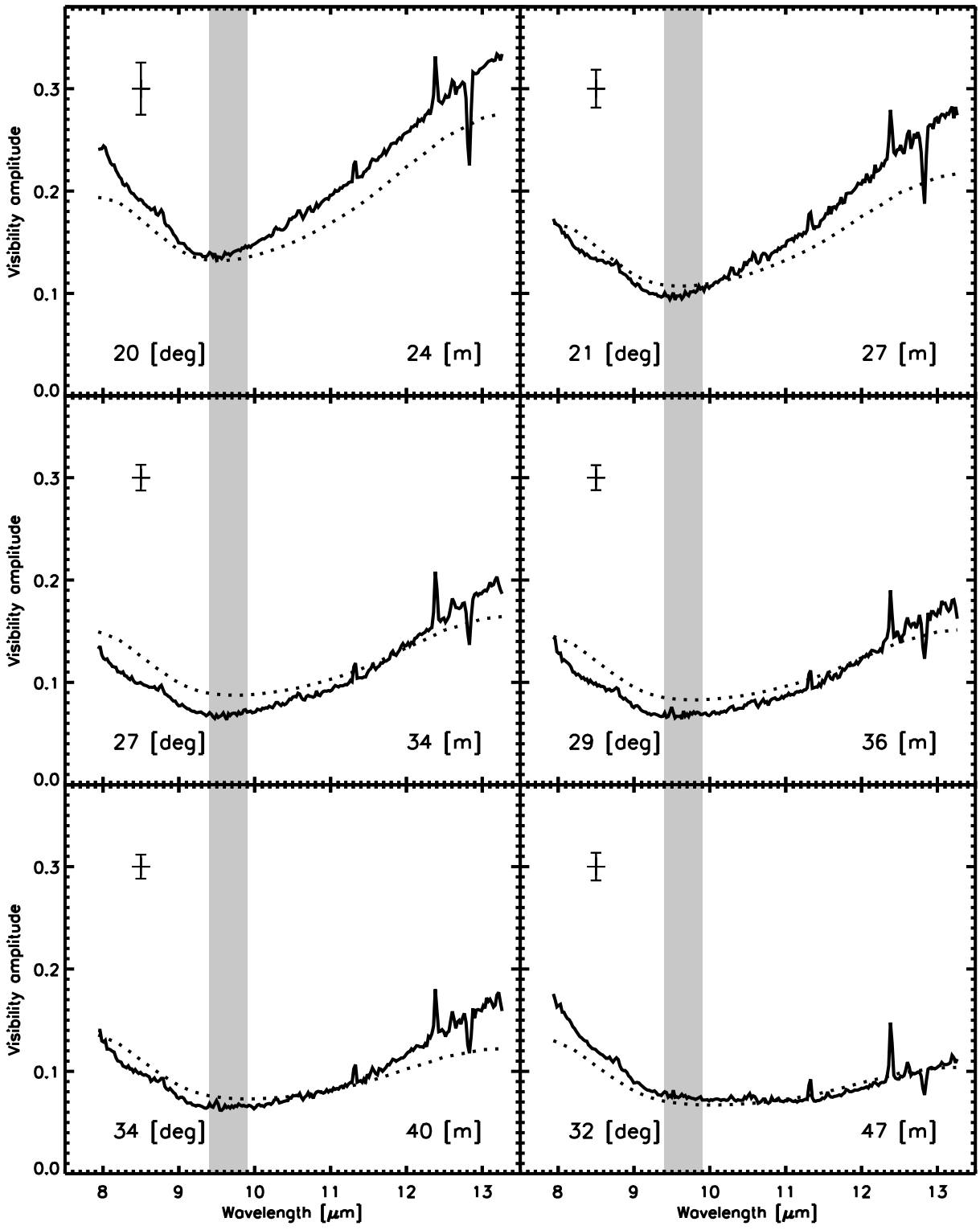

Figure 3.6 — Each panel displays the calibrated visibility amplitude of MWC 349A as function of wavelength for one observed (u,v) point. The position angles and projected length of the employed baselines are indicated in the lower left and right corners of each panel. Also indicated is the uncertainty for each measurement, derived from the scatter of the calibrators in that night. The gray areas indicate wavelength regions at which ozone in the Earth's atmosphere strongly influences the observed visibilities. The amplitudes measured in these wavelength regions are not included in our analysis. The dashed lines represent visibilities for our best model (see Section 3.3.1).

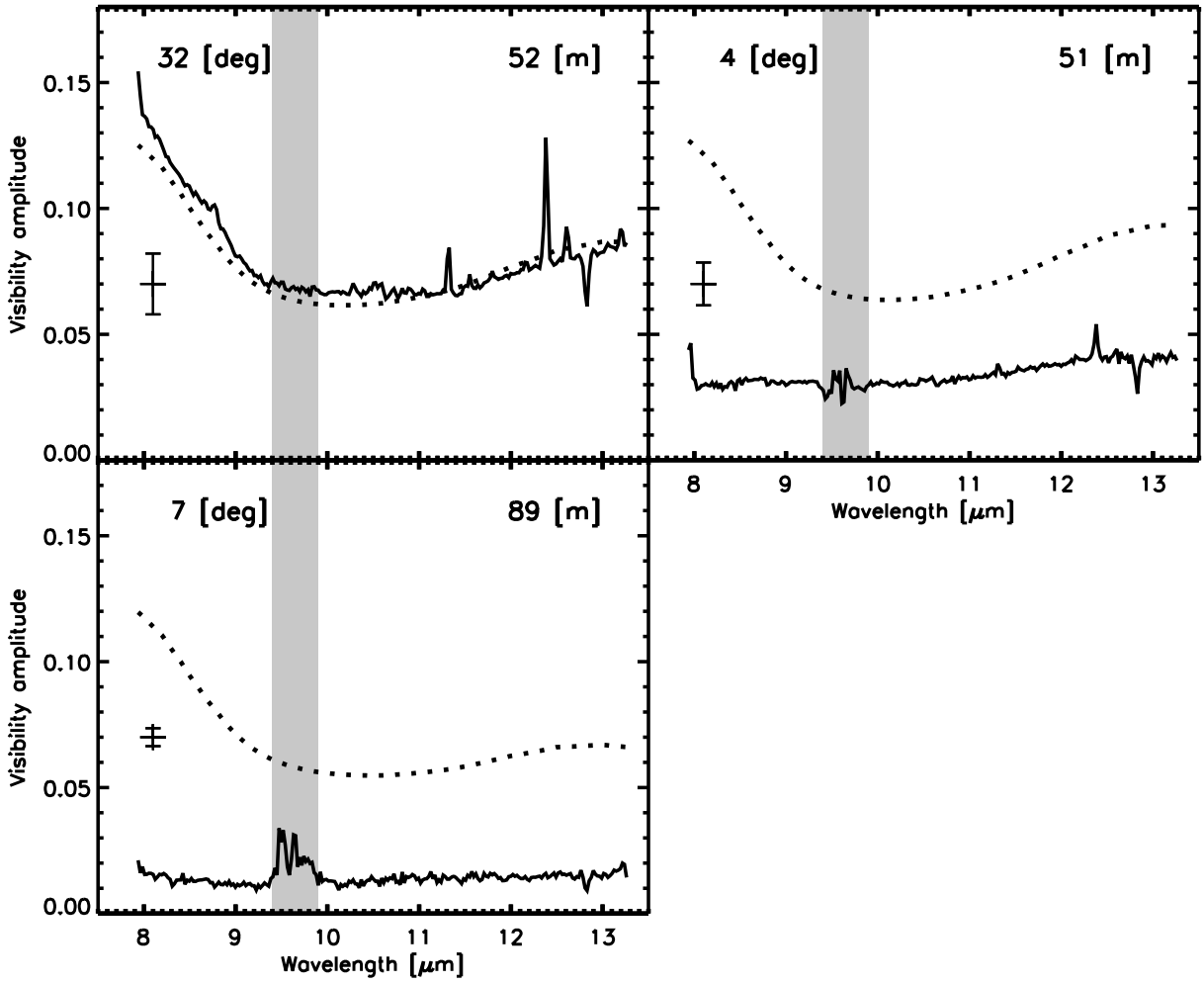

Figure 3.7 — As Figure 3.6, with each panel displaying the calibrated visibility amplitudes as function of wavelength for 3 other (u,v) points from longer baselines. Note the different scale in these panels relative to the panels in Figure 3.6. Also note the strong difference between the visibility amplitude at angles of $\sim 30^\circ$ and $\sim 0^\circ$. The dashed lines represent our best model. The model does not have a directional dependency, so it cannot reproduce the visibilities for the (u,v) obtained at small position angles, which also have not been included in the fits.

and short wavelength regimes of the spectrum, while at wavelengths around $\sim 9.7\,\mu$m one probes *hotter* layers higher above the mid-plane. For these layers the Wien cutoff of the black-body radiation happens at greater radii. This also means that the disk appears bigger around $\sim 9.7\,\mu$m, which reduces the measured visibility amplitude at these wavelengths. See also van Boekel et al. (2005) for a discussion on this subject.

For MWC 349A the rise in visibility amplitudes at longer wavelengths is more pronounced than for Herbig Ae/Be stars. For Herbig Ae/Be stars the dust disk is strongly heated at the inner rim, and depending on whether it is a flaring or non-flaring disk the rest of the disk is more or less in the shadow of the inner rim. In case of MWC 349A the central star with its high flux at short wavelengths generates an H II region around it. This H II region in turn illuminates the dust disk from above and below the disk. This heats up the outer layer of the disk out to distances which are normally in the shadow of the inner rim and cold. Therefore, for the

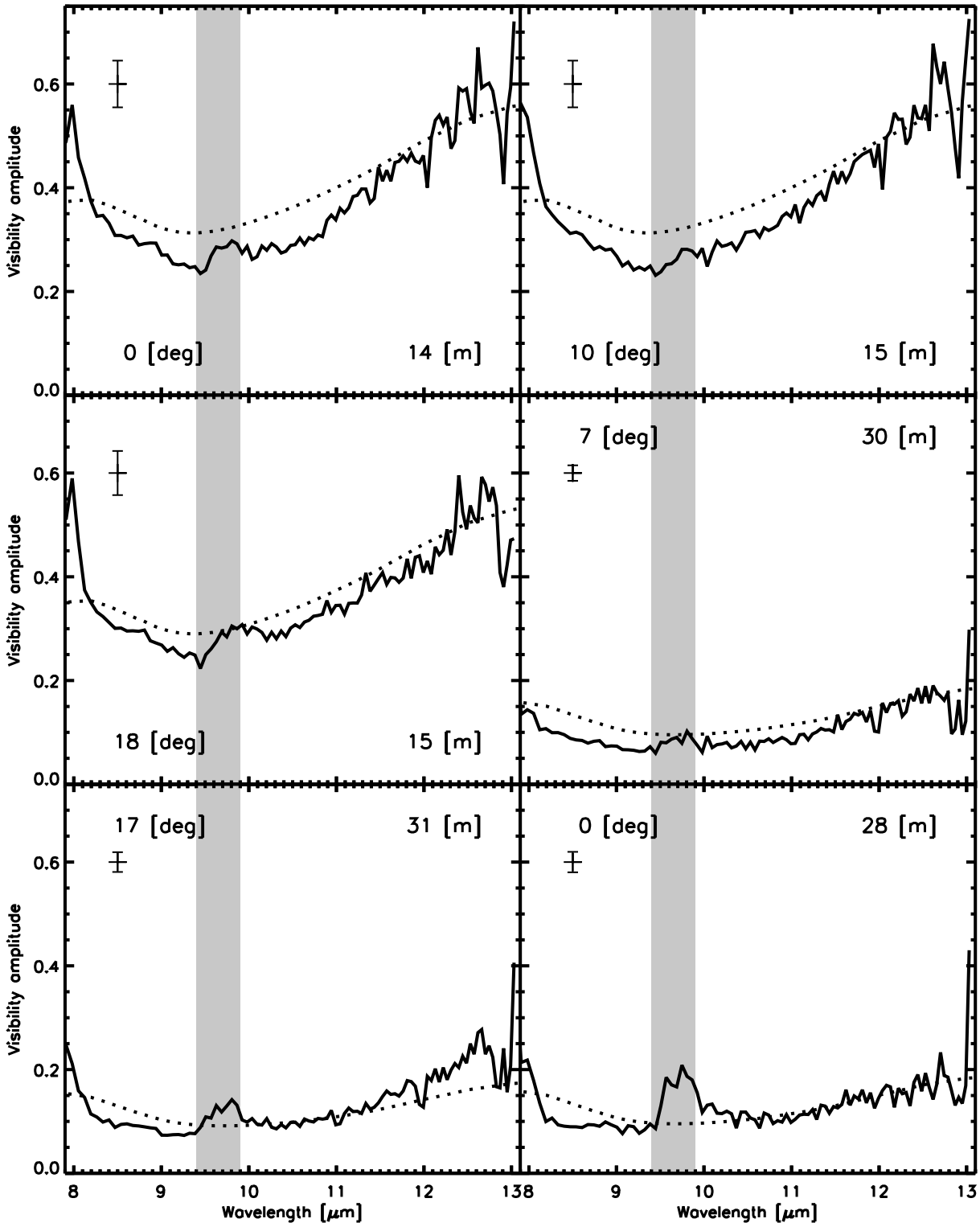

Figure 3.8 — As Figures 3.6 and 3.7. These six visibilities have been obtained using the ATs on the 16m and 32m baselines, covering position angles from $\sim 0°$ to $\sim 30°$. Each panel displays one calibrated visibility amplitude of MWC 349A obtained in Sci_Phot mode using the PRISM.

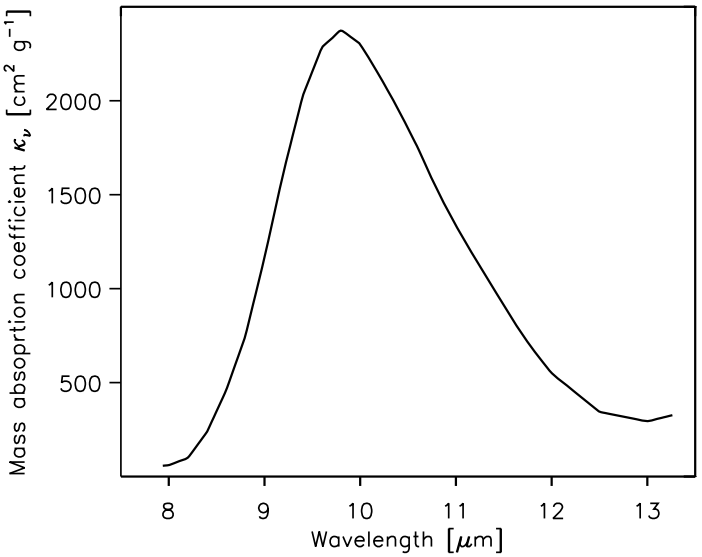

Figure 3.9 — Mass absorption coefficient κ_ν (opacity) of amorphous silicate as a function of wavelength in the pass-band of MIDI. The bulk of the flux in our model originates from the $\sim 300\,\mathrm{K}$ warm extended body whose SED is mainly shaped by the emission of amorphous silicate over almost all of the pass-band, along with amorphous silicate absorption around $9.7\,\mu$m.

case of MWC349A, MIDI probes the proto-planetary disk which has a substantial temperature difference between the layers higher above the midplane and layers close to the midplane. This temperature profile with height exists out to large radial distances.

To test this hypothesis we constructed as simple a model as possible, in which the brightness distribution of the circumstellar disk is represented by two black bodies at different temperatures, whose surface brightness decreases as a power law with $e^{-\frac{r}{\alpha}}$, where 'r' represents the radial distance and 'α' the free parameter determining the size of the black body. We chose this brightness distribution instead of a Gaussian as the temperature of the circumstellar disk decreases radially and assuming only two bodies at two different temperatures might be over-simplified. The gradual decrease in temperature with radius will result in a more "peaked" brightness distribution as represented by a Gaussian and might be better represented by the chosen distribution.

As well as the temperatures and the radial extent of the two bodies, three other free parameters enter the fit. These include the column density of silicate seen by MIDI in the upper layers of the disk. This column density determines the effective shape of the spectra emitted by the silicates in the MIDI pass-band. If the column density is low then the spectral effect due to silicate is strongest. With increasing column density the emission becomes optical thick, first in the middle of the MIDI passband, and later at the borders, until the silicates emit black-body radiation. The second parameter describes the ratio between the radiation originating from the silicates and pure black body radiation, i.e from smaller dust particles. Note that this spectral effect due to silicate emission is only included in the larger, more extended body, as silicates would not survive in the hotter smaller component. The final parameter describes the column density in a cold screen of amorphous silicates through which we see the disk. This parameter, however, does not influence the observed visibility amplitudes, as the visibility represents the ratio between the correlated and the uncorrelated flux. It does, however, influence the shape of the SED derived from the simulated bodies. For the fitting we used the lower S/N SED obtained by the 8m UT telescopes rather than the high S/N SED obtained from the ISO satellite,

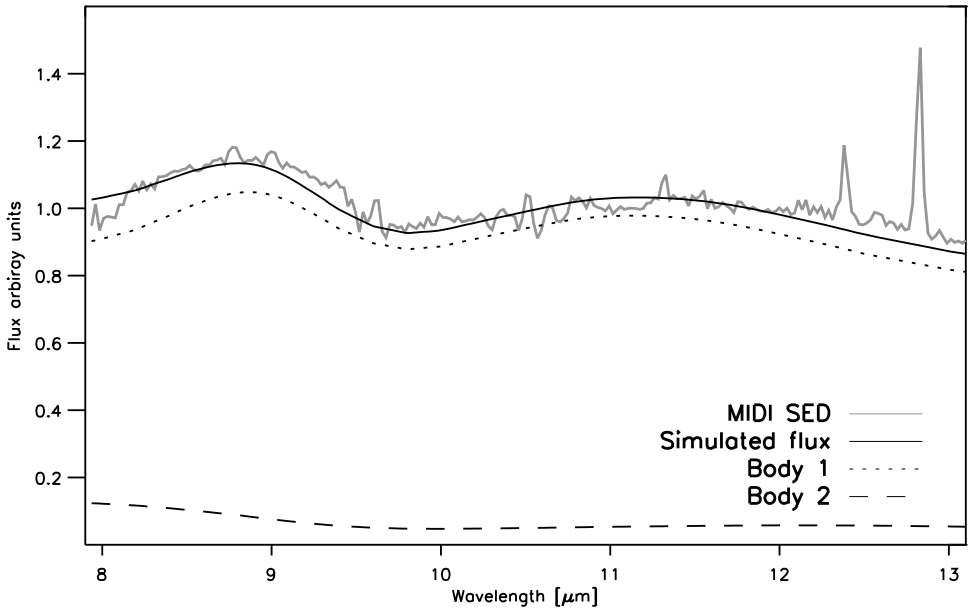

Figure 3.10 — Spectrum of MWC 349A obtained by MIDI using the UT's. Also shown as dashed line is the best fit to the visibility amplitudes and this SED.

because the beam-size of the latter is considerable bigger and therefore contains a less clean spectrum of MWC 349A. We did not attempt to calibrate the MIDI SED on an absolute scale as the extinction is not known precisely enough. Therefore the parameter found for the column density for silicate has only a limited physical meaning. Note that we included neither an inner hole, nor the star itself in our model. These were not needed as the inclination of the disk is thought to be around $\sim 70^{\circ}$, obscuring our view of the star and the inner region cleaned of dust by the intense radiation. We may, however, see one hot wall of the inner rim, which we represented here as the small hot body. The inner rim represents the inner surface of the dust disk which sees the star directly and the innermost radius where dust can survive. A simultaneous fit to the visibility amplitude in all MIDI bands (excluding the wavelengths where emission lines have been found and the wavelength region influenced strongest by Earth's atmosphere) and the scaled SED of MWC 349A in the MIDI pass-band, was carried out. We did not use an absolute scale for the SED because the absorption towards MWC 349A is not known precisely enough to further constrain the fit. Figure 3.10 displays the SED of MWC 349A in the wavelength band of MIDI, over-plotted with the fit of two black-bodies plus the effect from the silicate emission in the disk and absorption. As MWC349A has an almost edge-on disk one expects to see a certain amount of silicate in absorption as the emission from the warm disk will be seen through colder

Table 3.2 — The parameters derived from the χ^2 fit to the continuum visibility amplitudes and the SED measured by MIDI. The values in AU are given for an assumed distance of 1.2 kpc. See Section 3.3.1 for a discussion on the uncertainties.

Parameter	Best fit value
T_1	310 [K]
Surface brightness decreased by e^{-1}	0.12 [″]
Surface brightness decreased by e^{-1}	150 [AU]
ratio emission silicates/pure black body	0.21
T_2	1700 [K]
Surface brightness decreased by e^{-1}	0.0005 [″]
Surface brightness decreased by e^{-1}	0.7 [AU]

material in the outskirts of the disk. In Figures 3.6, 3.7, and 3.8 the model visibility amplitudes obtained from the fit are shown as dashed lines along with the measured visibility amplitudes from MIDI. The parameters, which fit the SED and visibility amplitudes best, are printed in Table 3.2.

Although it is clear that there is a strong directional dependency of the visibility amplitudes (see Figure 3.7 and references mentioned in the introduction), we kept this simple model with only a radial dependence of the visibilities because it was only possible to obtain measurements at position angles between $\sim 0^\circ$ and $\sim 30^\circ$. With the position angle of MWC 349A's elongation axis being $\sim 100^\circ$ degrees this means that it is not possible to get a reliable axial ratio. Note that the visibility amplitudes at baselines of 16 m and 32 m show only a very weak dependence on position angle, while the visibilities at baseline of ~ 50 m show a strong dependence. This means that the directional dependency is more important for the smaller hotter component than for the colder extended component. We estimate from the use of slightly different brightness distributions that the size parameter derived for the colder body is fairly robust $\sim 30\%$ while the size of the smaller body is only an order of magnitude estimate. The temperature of the colder (~ 300 K) is fairly well constrained by the flat SED of MWC 349A in the N band. The temperature of the smaller body is found vary between 1000 - 1800 K for different models. The ratio between the emission by silicates and pure black body radiation is a function of the chosen mass absorption coefficient, which we assumed to be that of small amorphous silicate grains. Finally, we find that the density of amorphous silicate along the line of sight is so low that its emission does not become optically thick. This finding is not surprising as the silicate resonance is the feature in our model which is mainly responsible for reproducing the characteristic observed visibility amplitude change with wavelength.

3.3.2 Hydrogen lines

The observed visibilities show a rich structure as a function of wavelength, due to the presence of strong emission lines. This makes it possible to independently probe the sizes and geometries of the disk, and the regions in which the hydrogen recombination lines originate. The MIDI visibility amplitudes and phases, for which one (u, v) sample is shown in Figure 3.4 and Figure

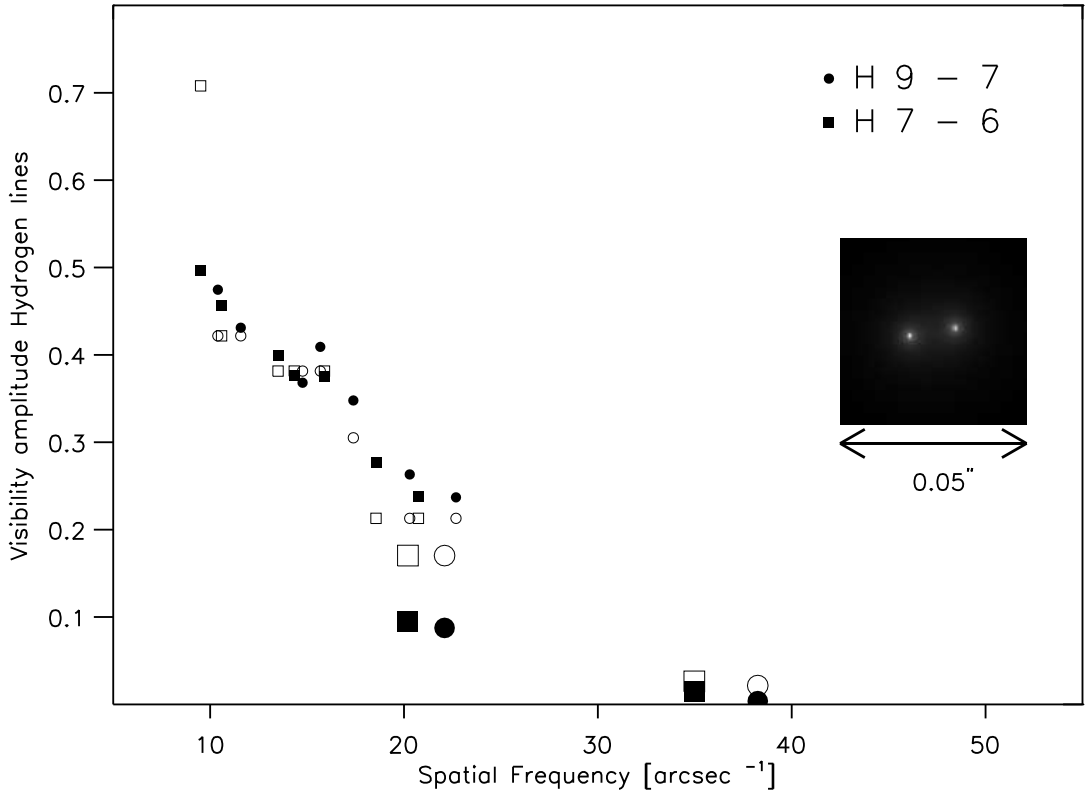

Figure 3.11 — Visibility amplitudes of the hydrogen recombination lines plotted as a function of spatial frequency. The filled squares indicate visibilities measured for the H 7-6 line and the open squares indicate visibilities measured for the H 9-7 line. Most visibilities have been obtained at wavelengths with position angles of $\sim 30°$. The bigger symbols have been obtained at an position angle of $\sim 0°$. The closed symbols represent the measurements, and the open symbols the calculated visibility amplitudes for our best fitting model for the hydrogen lines. The small pictogram shows the sky brightness distribution of this model (see Section 3.3.2)

.

3.5, provide information on a number of strong emission lines. We indicated in these plots the positions of all hydrogen lines which lie in the passband of MIDI.

In order to obtain the visibility amplitudes for the emission lines, the flux from the continuum has to be subtracted at the wavelengths of the emission lines in the correlated, and uncorrelated flux. The visibility $V_{\rm line}$ is then obtained by dividing these two quantities,

$$V_{line} = \frac{\mathrm{Cor_{line}} - \mathrm{Cor_{cont}}}{\mathrm{Pho_{line}} - \mathrm{Pho_{cont}}}, \tag{3.1}$$

where 'line' indicates a measurement of the total flux in the wavelength channels of a line and 'cont' indicates flux measurements in the adjacent continuum channels interpolated to the

Table 3.3 — Parameters derived from the fit to the visibility amplitudes of the H 7-6 and H 19-7 lines. See Section 3.3.2 for a discussion on the uncertainties.

Parameter	Best fit value
Distance of the emitting regions from each other	18 [mas]
Power law index α	1.2

wavelength of the emission line. 'Cor' stands for a measurement of the correlated flux and 'Pho' for the measurement of the total flux. This equation only holds if there is no differential phase between the continuum and the emission line, otherwise one has to calculate the complex visibility including the differential phase. As the phase differences between the lines are relatively small (see Figure 3.5) this can, at the level of the accuracy of our data, be ignored.

Figure 3.11 shows the visibility amplitudes of the two strongest hydrogen recombination lines in the MIDI band, H 7-6 and H 9-7, as a function of the spatial frequency. Note that although H7-6 is blended with H 11-9, which has a flux about ten times lower, we did not correct for this blending. From a comparison of the high visibilities found in the hydrogen lines with the significantly lower visibilities found in the continuum, it is clear that the region from which the hydrogen emission lines originate is a much more compact region than the region from where the continuum emission originates. This can place the emission of these hydrogen lines in the same area as the hydrogen recombination line masers, found at 40 AU in the disk (Martin-Pintado et al. 1989; Thum et al. 1994b). Recent very high S/N ratio observations of the H30α recombination line at 231.9 GHz confirmed these measurements (Weintroub et al. 2008) .

To better understand the distribution of the emission lines in the MIDI passband we create a simple model to reproduce the measured visibility amplitudes. It has been found by the authors mentioned above that most maser activity comes from two areas, each displaced by ~ 0.024 arcsec from the center of MWC 349A. We therefore create a model with two emitting bodies. As free parameters we have the separation of the two bodies from each other and the power law exponent α with which each body decreases in luminosity with radius; $r^{-\alpha}$. The power law index is assumed to be the same for both bodies, and the model is point symmetric around the center of MWC 349A. The last parameter is the position angle of the line which connects these two bodies, which we keep fixed to 100°, the same position angle found observationally for the disk, because we have only a limited number of measurements. Also previous observations suggest that the hydrogen emission line regions have a similar position angle as the disk, which is to be expected if the masers originate from the upper hot layers of the disk (Weintroub et al. 2008). The best fitting parameters are shown in Table 3.3 and the visibility amplitudes inferred are displayed as open symbols in Figure 3.11. Also the sky brightness of our model is shown as an insert in this figure. As in Section 3.3.1 we estimate the uncertainties in the derived parameters by fitting slightly different models to the visibility amplitudes. We estimate for the two parameters shown Table 3.3 an uncertainty of 50%.

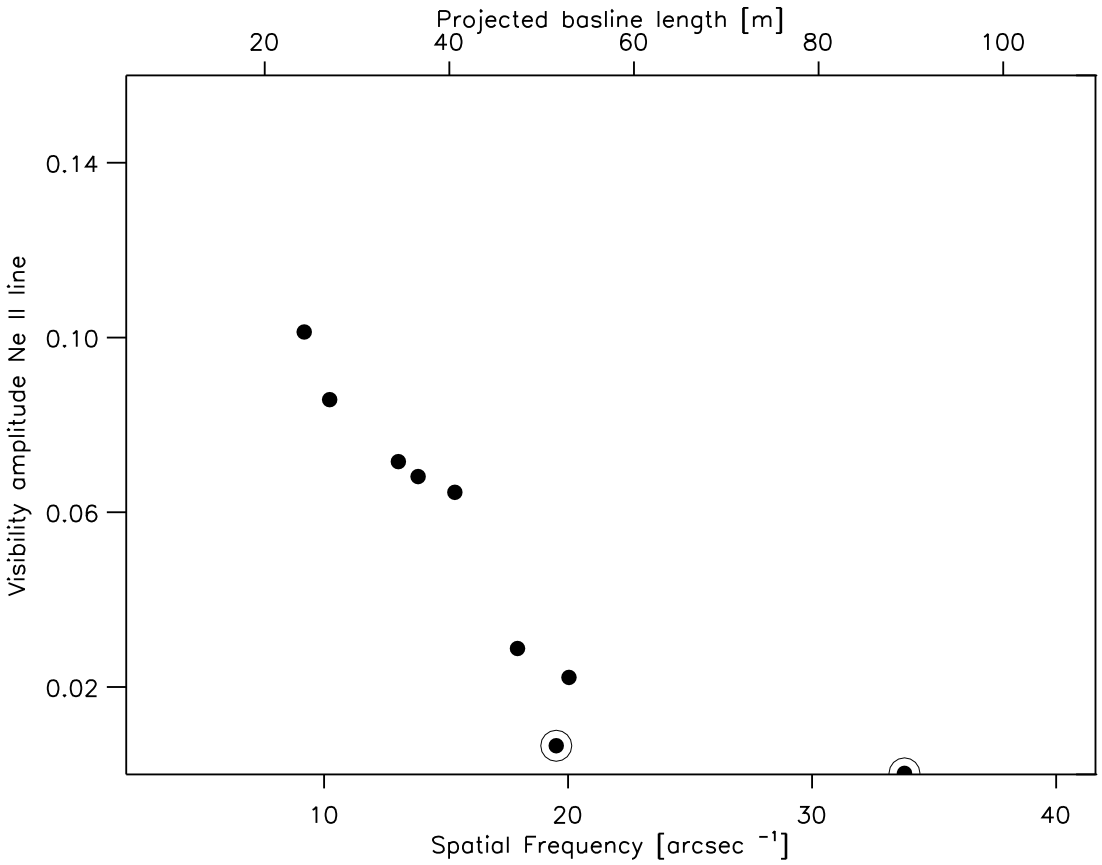

Figure 3.12 — Visibility amplitudes as determined for the [Ne II] line using Equation 3.1 plotted as function of spatial frequency. length. As for the visibilities of the hydrogen lines, most have been obtained at wavelengths with position angles of $\sim 30°$. The symbols which are surrounded by an open circle have been obtained at an position angle of $\sim 0°$.

3.3.3 Forbidden lines

The observed visibility amplitudes decrease at the positions of the forbidden lines [Ne II] 12.81 μm and [Ar III] 8.99 μm, respectively (Figure 3.4). A similar drop would be expected at the position of SIV 10.51 μm, but this line is blended with a strong hydrogen recombination line. Using Equation 3.1 the visibilities in the [Ne II] are calculated and plotted as a function of projected baseline length (i.e. spatial frequency) in Figure 3.12. The low values indicate that the [Ne II] emission is more extended than the hydrogen emission region and the disk emission region at the position angle probed, as expected in models in which the forbidden lines are formed in a wind that originates from the disk. Here we make no attempt to model the brightness distribution of the forbidden lines because the measured visibilities are low and represent the high spatial frequency variations in a brightness distribution with large spatial extent. In the future we intend to used the approach by Alexander (2008) who developed a model for [Ne II] around low mass stars. Since this model is scale free, it can be adapted for MWC 349A.

3.4 Discussion

The simple modelling of the circumstellar disk in Section 3.3.1 allows us to draw some interesting conclusions about the circumstellar material of MWC 349A. The overall shape of the visibility amplitudes with wavelength shows a decrease from short wavelengths towards 10 μm and a rise towards the longest wavelengths, something which could be explained by the influence of amorphous silicates in the disk. This feature also tells us something about the temperature structure of the disk. From the inner radius towards a radius of a few hundred AU the temperature in the disk has to have a strong gradient with height above the mid-plane and the temperature of the disk surface decreases less quickly with radius as for low mass stars.

A change of temperature with disk-height also exists in disks around T-Tauri stars ($M < 2M_{\odot}$) and Herbig AeBe stars ($2 < M_{\odot} M < 8M_{\odot}$). For these stars, however, the circumstellar disk at larger radii can be self-shadowed, and the distance from the star towards the outer parts of the disk, and the angle under which the star is seen by the disk, limit the maximum temperature reached at the surface of the disk at larger radii. This limits the overall contribution to the SED and visibility amplitudes in the N-band of the outer parts of the disk.

Using the models by Dullemond (2002) and Dullemond & Dominik (2004) we tested these assumptions about the disk temperatures heated by a central star. In these models the vertical structure of the disk is determined by hydrostatic equilibrium; dust sublimation creates an inner hole and an iterative process is used to obtain a solution for the temperature profile based on radiative transfer modeling. We have not been able to reproduce the observed visibility amplitudes and SED shape. This is expected as these models have been designed to represent the disks around low to medium mass stars, with the central stars as the main luminosity source. The presence of an ionized region around the central star would however naturally explain the assumed disk temperature structure out to large radii as it would illuminate the disk from *above* and *below*, and would be visible from the disk also at large radii. Our disk modelling shows therefore indirectly, as already shown by the low termination velocity of the wind (50 km s^{-1}), the presence of a H II region around the central star of MWC 349A. Currently we are implementing the effect of a Strömgren-sphere into the model by Dullemond (2002).

What can we say about the mineralogy of the disk? Having found that the measured visibility amplitudes can be modelled using small unprocessed amorphous silicate grains, does not mean that this is the dominant species in the disk. More processed species may not leave a signature in the visibility amplitudes as these bigger grains settle down towards the mid-plane of the disk, where they are difficult to observe, due to the optical depth and reduced temperature.

The derived size for the disk at 300 K is in agreement with what is found by Danchi et al. (2001), taking into account the smaller wavelengths used by these authors, and the resulting greater sensitivity to hotter structures. They found linear sizes of 44 AU and 57 AU at 1.65 μm and 2.27 μm, respectively. Our estimate of the decrease of the disk brightness to e^{-1} at 150 AU does however only refer to the brightness distribution along a position angle of $\sim 30°$. As explained above we did not include any directional dependency in our model, even if it is evident from earlier studies (e.g Danchi et al. 2001) that this should be present. The relatively small dependence of the lowest spatial frequencies (larger structures) on the position angle (Figure 3.8) and the strong dependency of the high spatial frequencies (smaller structures) on the position angle (Figure 3.7) shows that the innermost, hottest parts of the disk, can be interpreted as observing the hot inner wall of the inner rim which is directly illuminated by the central star.

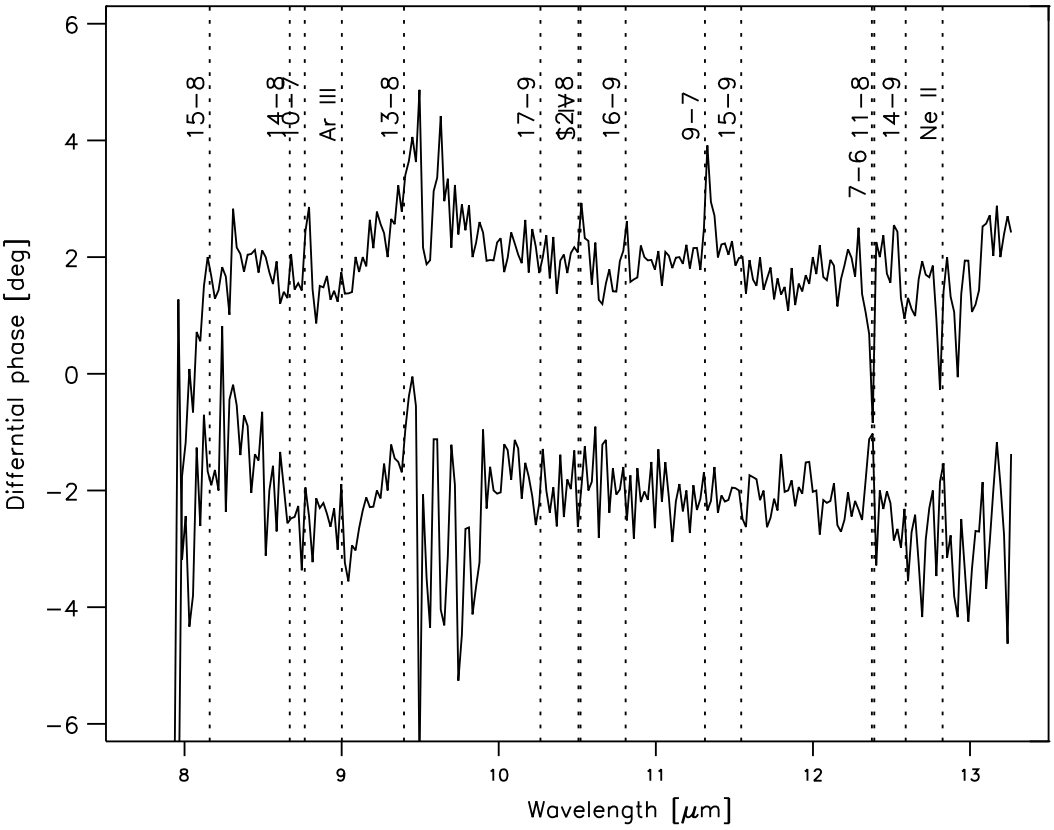

Figure 3.13 — The visibility phases of two (u,v) points. The upper line (moved up by 3 degrees) represents the differential phase obtained at a (u,v) point with a angle of $\sim 32^\circ$ and a projected baseline length of 52m. The lower line (moved down by 3 degrees) represents the differential phase obtained at a (u,v) point with a position angle of $\sim 4^\circ$ and a projected baseline length of 51m. This should be compared to the visibility amplitudes displayed in Figure 3.7.

In Section 3.3.2 we modeled the visibility amplitudes of the H 7-6 line at 12.36 μm and the H 9-7 line at 11.3 μm with a model consisting of two spherical bodies, separated by 18 mas from each other. This model is consistent with these hydrogen lines being emitted in the same region as hydrogen lines with higher n. Our model does not represent the directional dependency of the visibility amplitudes of the emission lines very well. This may be the result of a small mismatch between the position angle of 100° which we fixed in our model, and the real angle. Furthermore, our model may be too simplistic. Even if the bulk of the emission in the hydrogen lines comes from two regions, there is also fainter emission from a bar between the two spots which we have not modeled (see Weintroub et al. 2008).

The phase offset between the lines and the continuum emission shows that there is a small

position offset between the center of the continuum emission and the emission from the hydrogen lines. This is consistent with the picture that the emission lines originate on the "surface" of the inclined circumstellar disk, which produces the offset between the continuum emission and the line emission in the N-S direction, due to the E-W orientation of the circumstellar disk. In this picture there should be little or no offset along the E-W direction for the hydrogen emission. Indeed the differential phase of the two emission lines relative to the continuum for the (u,v) point with a position angle of $\sim 32^\circ$ and a projected baseline length of 52m, is bigger than for the measurement at the (u,v) point of a position angle of $\sim 4^\circ$ and a projected baseline length of 51m (see Figure 3.13). For the latter measurement the phase offset between the H 7-6 line and the continuum is barely detectable. Note however the lower S/N ratio for the latter differences between the continuum flux and the emission lines represent a direct confirmation that there is a small but significant difference in position between the centroid of the continuum flux and the hydrogen emission. This would have been difficult to establish if observations of the continuum and the maser activity would have been done in different observations.

We performed no modeling of the visibility amplitudes and differential phases found for the forbidden lines for reasons explained in Section 3.3.3. We will however in the future try to interpret the measurements for the [Ne II] line emission using the approach developed by Alexander (2008).

3.5 Summary and future work

In this chapter we presented high spatial resolution observations of MWC 349A obtained with the VLTI and MIDI. We showed that the measured visibility amplitudes can be successfully modelled using two black bodies, one hot and small, and another colder and extended, with the colder (300 K) body showing a clear signature of amorphous silicate. We argue that the smaller, hotter body can be interpreted as the inner rim of the disk, which is directly illuminated by the central star. We further argue that the strong silicate feature seen in the visibility curves over all but the highest spatial frequencies is an indication of a strong temperature variation with height in the circumstellar disk. This differentiates this disk around the massive 30 $M_\odot$ star from disks around intermediate and low mass stars, where the silicate resonance feature is seen to a much lesser extent, and where the gradient in disk temperature has a strong radial dependence. Our explanation for the temperature variation with disk height is the presence of an ionized region around the central star, which illuminates the disks from below and above. The use of more physically realistic models should confirm this picture and reveal the dimensions of the different components. It will also reveal the extent to which crystalline silicates are important. Furthermore, we plan to use the phase information obtained by MIDI after their correction for the earth atmosphere using the approach of Tubbs et al. (2004).

We show that the visibility amplitudes found in the hydrogen emission lines can be interpreted by modelling the emission as coming from two regions which are few tens of AU apart, and could represent the inner parts of the circumstellar disk. This is consistent with what is found at radio wavelengths for hydrogen maser lines. Our differential phase measurements of the lines show that the centroid of the continuum emission could come from the same region as

the hydrogen line emission, while there exists a small offset which we will attempt to quantify in a future work. This ties the optical center of MWC 349A firmly together with the center seen in the radio regime.

A further step will be the modeling of the wind, using the constraints from the visibility amplitudes and phases of the forbidden lines. This should ultimately lead to a comprehensive view of the environment of MWC 349A, based on the many complementary data sets that have been obtained for this unique object.

Acknowledgments

We thank Richard Alexander, Kees Dullemond, and Roy van Boekel very much for useful discussions.

APPENDIX

Table A.1 — Log of the MIDI observations of MWC 349A.

Nr.	Target	Night	UT [h:m]	ra [h:m:s]	Dec [d:m:s]	Baseline [m]	Base proj. [m]	Mode	Disp. elem.	angle [deg]
0	HD120404	2005-05-26	22:57	13 51 47.5	-69 24 4.6	46.6	42.6	HIGH_SENS	P	78.8
1	HD112213	2005-05-27	01:06	12 55 19.4	-42 54 56.1	46.6	45.5	HIGH_SENS	P	50.0
2	HD120404	2005-05-27	02:02	13 51 47.4	-69 24 4.2	46.6	39.6	HIGH_SENS	P	42.6
3	HD112213	2005-05-27	02:54	12 55 19.3	-42 54 56.1	46.6	41.6	HIGH_SENS	P	36.3
4	HD120404	2005-05-27	03:40	13 51 47.5	-69 24 4.3	46.6	36.3	HIGH_SENS	P	22.9
5	Alp_Lyr	2005-05-27	05:30	18 36 56.4	38 47 3.1	46.6	24.1	HIGH_SENS	G	23.3
6	Alp_Lyr	2005-05-27	05:52	18 36 56.4	38 47 3.1	46.6	26.8	HIGH_SENS	G	24.1
7	Del_Lyr	2005-05-27	06:16	18 54 30.2	36 53 56.0	46.6	28.1	HIGH_SENS	G	26.7
8	Del_Lyr	2005-05-27	06:38	18 54 30.2	36 53 56.0	46.6	30.6	HIGH_SENS	G	27.5
9	13_Lyr	2005-05-27	07:04	18 55 20.2	43 56 47.2	46.6	31.5	HIGH_SENS	G	22.2
10	MWC349A	2005-05-27	07:30	20 32 45.6	40 39 37.3	46.6	24.3	HIGH_SENS	G	20.6
11	MWC349A	2005-05-27	07:53	20 32 45.6	40 39 37.3	46.6	27.0	HIGH_SENS	G	22.0
12	Alp_Lyr	2005-05-27	08:17	18 36 56.5	38 47 2.8	46.6	40.4	HIGH_SENS	G	34.5
13	Alp_Lyr	2005-05-27	08:39	18 36 56.5	38 47 2.8	46.6	41.7	HIGH_SENS	G	36.6
14	MWC349A	2005-05-27	09:04	20 32 45.5	40 39 36.3	46.6	34.5	HIGH_SENS	G	27.3
15	MWC349A	2005-05-27	09:28	20 32 45.5	40 39 36.3	46.6	36.6	HIGH_SENS	G	29.4
16	Gam_Cyg	2005-05-27	09:57	20 22 13.7	40 15 23.8	46.6	39.7	HIGH_SENS	G	33.3
17	MWC349A	2005-05-27	10:23	20 32 45.6	40 39 37.6	46.6	40.6	HIGH_SENS	G	34.6
18	hd116870	2005-05-27	23:48	13 26 43.5	-12 42 27.9	56.6	53.0	HIGH_SENS	P	77.7
19	hd116870	2005-05-28	01:25	13 26 43.5	-12 42 27.6	56.6	55.2	HIGH_SENS	P	65.5
20	hd100407	2005-05-28	02:53	11 33 0.1	-31 51 27.9	56.6	49.9	HIGH_SENS	P	49.3
21	hd100407	2005-05-28	04:28	11 33 0.1	-31 51 27.0	56.6	42.1	HIGH_SENS	P	47.3
22	Alp_Lyr	2005-05-28	06:39	18 36 56.4	38 47 1.4	102.4	63.6	HIGH_SENS	G	34.9
23	13_Lyr	2005-05-28	07:06	18 55 20.1	43 56 46.1	102.4	61.7	HIGH_SENS	G	29.5
24	MWC349A	2005-05-28	07:33	20 32 45.5	40 39 37.2	102.4	47.4	HIGH_SENS	G	32.8
25	MWC349A	2005-05-28	07:55	20 32 45.5	40 39 37.2	102.4	52.9	HIGH_SENS	G	32.4
26	Alp_Lyr	2005-05-28	08:48	18 36 56.5	38 47 0.9	102.4	87.3	HIGH_SENS	G	41.5
27	MWC349A	2005-05-28	09:15	20 32 45.5	40 39 36.7	102.4	70.9	HIGH_SENS	G	34.5
28	MWC349A	2005-05-28	09:37	20 32 45.5	40 39 36.7	102.4	75.2	HIGH_SENS	G	35.8
29	MWC349A	2005-05-28	10:00	20 32 45.5	40 39 36.7	102.4	79.3	HIGH_SENS	G	37.3
30	MWC349A	2005-05-28	10:22	20 32 45.5	40 39 36.7	102.4	82.9	HIGH_SENS	G	38.9
31	Eps_Cyg	2005-05-28	10:49	20 46 12.8	33 58 14.0	102.4	89.2	HIGH_SENS	G	43.1
32	HD165135	2005-07-20	23:12	18 5 48.4	-30 25 29.2	62.5	41.3	HIGH_SENS	P	5.7
33	HD165135	2005-07-20	23:21	18 5 48.4	-30 25 29.2	62.5	42.9	HIGH_SENS	P	4.3
34	HD165135	2005-07-21	00:33	18 5 48.4	-30 25 29.1	62.5	53.4	HIGH_SENS	P	-4.7
35	HD178345	2005-07-21	01:57	19 10 1.7	-39 20 27.5	62.5	55.4	HIGH_SENS	P	-2.5
36	HD173484	2005-07-21	02:55	18 46 47.2	-29 37 54.0	62.5	61.6	HIGH_SENS	P	-16.4
37	HD165135	2005-07-21	03:43	18 5 48.5	-30 25 27.4	62.5	61.8	HIGH_SENS	P	-27.6
38	HD173484	2005-07-21	04:57	18 46 47.2	-29 37 53.4	62.5	60.4	HIGH_SENS	P	-32.4
39	GamCyg	2005-07-21	06:12	20 22 13.7	40 15 23.3	62.5	53.5	HIGH_SENS	G	0.9
40	MWC349A	2005-07-21	06:40	20 32 45.5	40 39 37.2	62.5	51.6	HIGH_SENS	G	4.1
41	hd150052	2005-08-24	23:22	16 38 47.7	-8 37 6.3	89.4	89.4	HIGH_SENS	P	7.8
42	HD157236	2005-08-25	01:40	17 23 21.5	-28 8 34.0	89.4	81.5	HIGH_SENS	P	-4.1
43	GamCyg	2005-08-25	02:51	20 22 13.7	40 15 24.4	89.4	88.7	HIGH_SENS	G	4.0
44	MWC349A	2005-08-25	03:25	20 32 45.5	40 39 37.4	89.4	89.3	HIGH_SENS	G	7.7
45	GamCyg	2005-08-25	03:54	20 22 13.7	40 15 24.3	89.4	89.2	HIGH_SENS	G	14.1
46	hd178345	2005-08-25	04:24	19 10 1.7	-39 20 26.8	89.4	74.2	HIGH_SENS	P	-19.8
47	HD123139	2006-05-25	23:15	14 6 41.0	-36 22 11.8	32.0	28.1	HIGH_SENS	P	54.9
48	HD150798	2006-05-25	23:56	16 48 39.9	-69 1 39.8	32.0	31.9	HIGH_SENS	P	88.3
49	HD150798	2006-05-26	01:17	16 48 39.9	-69 1 39.8	32.0	32.0	HIGH_SENS	P	68.9
50	HD150798	2006-05-26	01:32	16 48 39.9	-69 1 39.8	32.0	32.0	HIGH_SENS	P	65.3
51	HD150798	2006-05-26	02:58	16 48 39.9	-69 1 39.8	32.0	32.0	HIGH_SENS	P	45.3
52	HD150798	2006-05-26	03:38	16 48 39.9	-69 1 39.8	32.0	31.9	HIGH_SENS	P	36.1
53	HD150798	2006-05-26	04:19	16 48 39.9	-69 1 39.8	32.0	31.7	HIGH_SENS	P	26.8
54	HD150798	2006-05-26	05:27	16 48 39.9	-69 1 39.8	32.0	31.0	HIGH_SENS	P	11.3
55	HD146051	2006-05-26	07:27	16 14 20.7	-3 41 39.6	32.0	26.9	HIGH_SENS	P	18.2
56	HD123139	2006-05-26	07:54	14 6 41.0	-36 22 11.8	32.0	13.5	HIGH_SENS	P	-45.9
57	MWC349	2006-05-26	08:51	20 32 45.4	40 39 36.8	32.0	30.3	SCI_PHOT	P	7.0
58	MWC349	2006-05-26	09:03	20 32 45.4	40 39 36.8	32.0	30.7	HIGH_SENS	G	8.8
59	MWC349	2006-05-26	09:57	20 32 45.4	40 39 36.8	32.0	31.8	SCI_PHOT	P	17.2
60	MWC349	2006-05-26	10:08	20 32 45.4	40 39 36.8	32.0	31.9	HIGH_SENS	G	19.0
61	EpsPeg	2006-05-26	10:34	21 44 11.2	9 52 30.0	32.0	31.9	SCI_PHOT	P	16.6
62	HD120323	2006-06-16	23:54	13 49 26.7	-34 27 2.8	16.0	15.9	HIGH_SENS	P	26.9
63	HD123139	2006-06-17	01:56	14 6 40.9	-36 22 11.8	16.0	15.6	HIGH_SENS	P	11.7
64	HD146051	2006-06-17	03:23	16 14 20.7	-3 41 39.6	16.0	16.0	HIGH_SENS	P	17.6
65	HD169916	2006-06-17	04:19	18 27 58.2	-25 25 18.1	16.0	15.5	HIGH_SENS	P	27.2
66	MWC349	2006-06-17	06:35	20 32 45.4	40 39 36.8	16.0	14.1	SCI_PHOT	P	-0.9
67	MWC349	2006-06-17	06:54	20 32 45.4	40 39 36.8	16.0	14.6	HIGH_SENS	G	2.2
68	EpsPeg	2006-06-17	07:21	21 44 11.2	9 52 30.0	16.0	13.8	SCI_PHOT	P	14.2
69	MWC349	2006-06-17	07:46	20 32 45.4	40 39 36.8	16.0	15.5	SCI_PHOT	P	10.4
70	MWC349	2006-06-17	07:58	20 32 45.4	40 39 36.8	16.0	15.6	HIGH_SENS	G	12.1
71	EpsPeg	2006-06-17	08:24	21 44 11.2	9 52 30.0	16.0	15.4	SCI_PHOT	P	15.3
72	MWC349	2006-06-17	08:39	20 32 45.4	40 39 36.8	16.0	15.9	SCI_PHOT	P	18.6
73	MWC349	2006-06-17	08:50	20 32 45.4	40 39 36.8	16.0	16.0	HIGH_SENS	G	20.3
74	EpsPeg	2006-06-17	09:16	21 44 11.2	9 52 30.0	16.0	16.0	SCI_PHOT	P	17.0
75	HD4128	2006-06-17	09:45	0 43 35.4	-17 59 11.8	16.0	14.2	HIGH_SENS	P	31.4
76	hd120323	2006-06-18	22:45	13 49 26.7	-34 27 2.8	16.0	30.4	HIGH_SENS	G	37.0
77	2Cen	2006-06-18	23:09	13 49 26.7	-34 27 2.8	32.0	31.0	SCI_PHOT	P	32.9
78	HD150798	2006-06-19	00:51	16 48 39.9	-69 1 39.8	32.0	32.0	HIGH_SENS	P	52.9
79	2Cen	2006-06-19	03:16	13 49 26.7	-34 27 2.8	32.0	26.4	SCI_PHOT	P	-2.1
80	HD150798	2006-06-19	04:01	16 48 39.9	-69 1 39.8	32.0	30.9	HIGH_SENS	P	9.2
81	HD169916	2006-06-19	06:12	18 27 58.2	-25 25 18.1	32.0	31.4	HIGH_SENS	P	13.7
82	MWC349	2006-06-19	06:38	20 32 45.4	40 39 36.8	32.0	28.8	SCI_PHOT	P	0.8
83	MWC349	2006-06-19	06:49	20 32 45.4	40 39 36.8	32.0	29.2	HIGH_SENS	G	2.6
84	EpsPeg	2006-06-19	07:15	21 44 11.2	9 52 30.0	32.0	27.7	SCI_PHOT	P	14.3
85	HD187642	2006-06-19	07:34	0 43 35.4	-17 59 11.8	32.0	21.0	HIGH_SENS	P	57.7
86	HD4128	2006-06-19	08:45	0 43 35.4	-17 59 11.8	32.0	25.3	HIGH_SENS	P	40.1
87	BetGru	2006-06-19	09:09	22 42 40.1	-46 53 4.5	32.0	32.0	SCI_PHOT	P	22.2
88	BetGru	2006-06-19	09:29	22 42 40.1	-46 53 4.5	32.0	31.8	SCI_PHOT	P	18.5
89	BetGru	2006-06-19	09:50	22 42 40.1	-46 53 4.5	32.0	31.6	SCI_PHOT	P	14.9

Bibliography

Alexander, R. D. 2008, MNRAS, 391, L64 54, 57
Altenhoff, W. J., Thum, C., & Wendker, H. J. 1994, A & A, 281, 161 38
Baldwin, J. E., Harris, C. S., & Ryle, M. 1973, Nature, 241, 38 38
Danchi, W. C., Tuthill, P. G., & Monnier, J. D. 2001, The Astrophysical Journal, 562, 440 39, 55
Dullemond, C. P. 2002, A & A, 395, 853 55
Dullemond, C. P. & Dominik, C. 2004, A & A, 417, 159 55
Gordon, M. A. 1992, The Astrophysical Journal, 387, 701 38
Hamann, F. & Simon, M. 1986, The Astrophysical Journal, 311, 909 38
Hofmann, K.-H., Balega, Y., Ikhsanov, N. R., Miroshnichenko, A. S., & Weigelt, G. 2002, A & A, 395, 891 39
Leinert, C., Graser, U., Przygodda, F., et al. 2003, Astrophysics and Space Science, 286, 73 39
Leinert, C., van Boekel, R., Waters, L. B. F. M., et al. 2004, A & A, 423, 537 45
Martin-Pintado, J., Bachiller, R., Thum, C., & Walmsley, M. 1989, A & A, 215, L13 38, 39, 53
Martín-Pintado, J., Gaume, R., Bachiller, R., Johnston, K., & Planesas, P. 1993, The Astrophysical Journal Letters, 418, L79 38
Meyer, J. M., Nordsieck, K. H., & Hoffman, J. L. 2002, The Astronomical Journal, 123, 1639 38
Planesas, P., Martin-Pintado, J., & Serabyn, E. 1992, The Astrophysical Journal Letters, 386, L23 38
Quirrenbach, A., Frink, S., & Thum, C. 2001, in ASP Conf. Ser. 242: Eta Carinae and Other Mysterious Stars: The Hidden Opportunities of Emission Spectroscopy, ed. T. R. Gull, S. Johannson, & K. Davidson, 183 38, 39
Tafoya, D., Gómez, Y., & Rodríguez, L. F. 2004, The Astrophysical Journal, 610, 827 38
Thum, C. & Martin-Pintado, J. 1994, in ASP Conf. Ser. 62: The Nature and Evolutionary Status of Herbig Ae/Be Stars, ed. P. S. The, M. R. Perez, & E. P. J. van den Heuvel, 265 38
Thum, C., Martin-Pintado, J., & Bachiller, R. 1992, A & A, 256, 507 38
Thum, C., Martin-Pintado, J., Quirrenbach, A., & Matthews, H. E. 1998, A & A, 333, L63 39
Thum, C., Matthews, H. E., Harris, A. I., et al. 1994a, A & A, 288, L25 38
Thum, C., Matthews, H. E., Martin-Pintado, J., et al. 1994b, A & A, 283, 582 38, 39, 53
Tubbs, R. N., Meisner, J. A., Bakker, E. J., & Albrecht, S. 2004, in Society of Photo-Optical Instrumentation Engineers (SPIE) Conference Series, Vol. 5491, Society of Photo-Optical Instrumentation Engineers (SPIE) Conference Series, ed. W. A. Traub, 588 57
van Boekel, R., Dullemond, C. P., & Dominik, C. 2005, A&A, 441, 563 47
Weintroub, J., Moran, J. M., Wilner, D. J., et al. 2008, ApJ, 677, 1140 53, 56
White, R. L. & Becker, R. H. 1985, The Astrophysical Journal, 297, 677 38